Comparative Numerical Studies of Scramjet Inlet Performance using k-ε Turbulence Model with Adaptive Grids

Ramesh Kolluru[1] and Vijay Gopal[1]
[1]BMS College of Engineering, Bangalore, Karnataka, India
*Corresponding author: BMS College of engineering, Bangalore 560 019, aero.g.vijay@gmail.com

Abstract: Scramjet inlet design remains as a key aspect for hypersonic flight. To assess the inlet design, the performance parameters namely; air-capture ratio, total pressure efficiency, inlet drag coefficient, and kinetic energy efficiency are evaluated and analysed. In the current study comparison of performance parameters is carried out by performing numerical computation of 2-D turbulent flow field for four different scramjet inlet geometries with two different free stream Mach number (M=4 and 5). The numerical computation is performed with the help of Femlab's finite element method tool "Comsol Multiphysics" using the "Turbulent High Mach Number Flow" module provided in it.
Keywords: Inlet ramp, Pardiso, Hypersonic

1. Introduction: Scramjet flight demands sustained combustion for producing required thrust to counter the enormous drag that prevails in hypersonic flight. The design of hypersonic inlet for scramjet-engine is pivotal to ensure stable combustion [9]. As the hypersonic flight exceeds Mach 5, the residence time of the air inside the combustion chamber drops to a very low value which engenders the difficulty of combustion, also, very low static pressure prevails at cruise altitude >20km which compounds to this difficulty. The inlet serves to counter this difficulty by slowing down the head stream and increasing the pressure to provide favourable flow conditions for combustion. It is therefore cardinal to study the inlet performance by evaluating multiple standard parameters which signify them. The current study involves comparison of performance parameters for scramjet inlet which are evaluated as a result of FEM computation of 2-D turbulent flow field around four different scramjet inlet geometries. The salient geometrical parameters which are varied are; inlet ramp contour and cowl angle. The design ensures to avoid any event of unstart [3] by restricting the internal contraction ratio of scramjet to be less than Kantrowitz limit [1]. The 2-D computation of turbulent flow is obtained by implementing high Reynolds number k-ε compressible turbulent formulation. The boundary and initial conditions are carefully selected to mimic the free stream conditions that pertain to a cruise altitude of 25km. The simulations were performed for both free stream Mach number 4 and 5. Thus from the obtained result, comparative studies of performance parameters are carried out by parameterising geometrical variables and free stream Mach number.

1.1 Inlet Performance Parameters: The vital inlet performance parameters [1], [11] which quantify mass capture, total pressure efficiency, kinetic efficiency and aerodynamic drag are described in the equations (1-4) with reference to **Figure 1**.

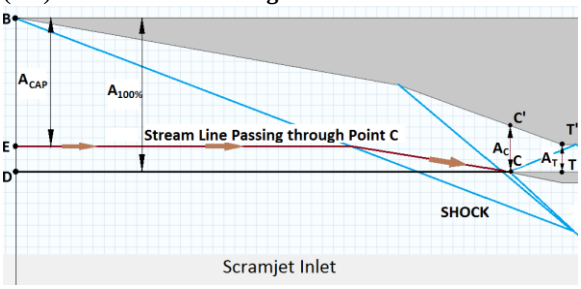

Figure 1: Scramjet inlet geometrical definitions

Air-capture ratio: $$m_c = \frac{A_{CAP}}{A_{100\%}} \quad (1)$$

Total pressure efficiency: $$\eta_P = \frac{P_{0T}}{P_{0\infty}} \quad (2)$$

Kinetic energy efficiency: $$\eta_{KE} = \frac{h_{0T} - h_T^*}{h_{0\infty} - h_\infty} \quad (3)$$

Inlet drag co-efficient: $$C_D = \frac{L_D}{\frac{1}{2}\cdot\rho_\infty \cdot V_\infty^2 \cdot A_{CAP}} \quad (4)$$

The subscript '0' indicates total quantities, '∞' refers to free-stream conditions and 'T' indicates line-averaged throat conditions for thermodynamic variables, while the superscript '*' represents final state of a variable subjected to an isentropic process such that $P^*=P_\infty$. The thermodynamic variable P, h and ρ have their usual meanings. Also 'V' represents velocity magnitude and 'A' area of cross section (in 2D whose units are in length). With Reference to **Figure 1** point 'C' indicates the tip of the cowl lip while points 'E' and 'D' lie on free-stream conditions (line DC is aligned in the direction of free-stream velocity) and the cross-sectional area A_{cap}, A_T, A_C and $A_{100\%}$ can be interpreted from the referred figure.

2. Inlet geometry: For the numerical study, inlet geometrical parameters such as inlet ramp contour and cowl angle (δ) are varied. The inlet ramp is either designed to be a double ramp **Figure 2** or a smooth second degree curve **Figure 3** while the cowl angle is either 0^0 or 10^0, which all to-gather provides four different combinations. To compare the performance parameters the throat area A_T is made constant (0.05m) and the final turning angle of the inlet ramp is also held constant of about 20^0 in all the four geometries. The internal contraction $c_i = \frac{A_C}{A_T}$ is depicted in **Table 1** and total contraction ratio $c_t = \frac{A_{100\%}}{A_T}$ in **Table 2** which is restricted below Kantrowitz limit [1]. The Inlet geometry with double ramp will be referred to as 'DR' while isentropic ramp as 'ICR'. It is to be noted that the nose and the vertex of cowl lip is constructed to be sharp without any radius of curvature.

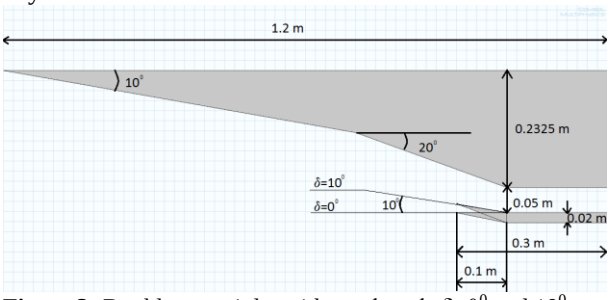

Figure 2: Double ramp inlet with cowl angle δ=0^0 and 10^0.

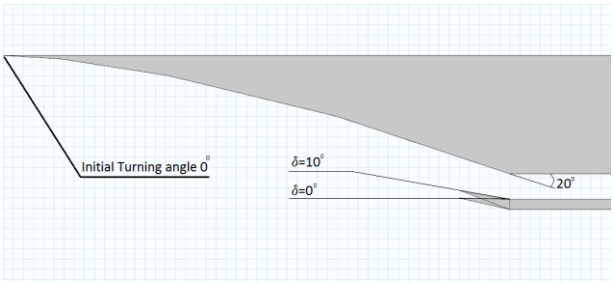

Figure 3: Isentropic compression ramp inlet with cowl angle δ=0^0 and 10^0 (other relevant dimensions are indicated in **Figure 2**).

c_i	DR	ICR
$\delta = 0^0$	1.726	1.666
$\delta = 10^0$	1.302	1.330

Table 1: Inlet internal contraction ratio $\frac{A_C}{A_T}$ depicted for all the four inlet geometries.

c_t	DR	ICR
$\delta = 0^0$	5.650	5.650
$\delta = 10^0$	5.302	5.302

Table 2: Inlet total contraction ratio $\frac{A_{100\%}}{A_T}$ depicted for all the four inlet geometries.

3. Governing equations of fluid: The FEM tool solves non-conservative form of compressible Navier-Stokes equation numerically. To account for turbulence in the flow field, additional transport equations are included which describe the energy interaction between eddies and free stream flow. The present numerical simulation uses high Reynolds number compressible k-ε turbulent model [2] which implements Favre averaging for fluctuating components. Finally to obtain closed form equations, the thermodynamic state relationship for ideal gas is used. The non-conservative forms of governing equations are described in equations (5-16):

Mass conservation:

$$\frac{\partial \bar{\rho}}{\partial t} + \bar{\rho}\cdot\nabla\cdot\left(\tilde{U}\right) + \left(\tilde{U}\cdot\nabla\right)\bar{\rho} = 0 \qquad (5)$$

Momentum conservation:

$$\bar{\rho}\left(\frac{\partial \tilde{U}}{\partial t} + \left(\tilde{U}\cdot\nabla\right)\tilde{U}\right) = \nabla\cdot\left[-\bar{p}\cdot\boldsymbol{I} + \left(\mu+\mu_T\right)\left(\left(\nabla\tilde{U}\right) + \left(\nabla\tilde{U}\right)^T - \frac{2}{3}\cdot\left(\nabla\cdot\tilde{U} - \bar{\rho}\cdot k\right)\cdot\boldsymbol{I}\right)\right] \qquad (6)$$

High Reynolds number k-ε compressible Turbulence transport equation:

$$\bar{\rho}\cdot\left(\frac{\partial k}{\partial t} + \left(\tilde{U}\cdot\nabla\right)k\right) = \nabla\cdot\left(\left(\mu + \frac{\mu_T}{\sigma_k}\right)\cdot\nabla k\right) + P_k - \mathrm{D}_k \qquad (7)$$

$$\bar{\rho}\cdot\left(\frac{\partial \varepsilon}{\partial t} + \left(\tilde{U}\cdot\nabla\right)\varepsilon\right) = \nabla\cdot\left(\left(\mu + \frac{\mu_T}{\sigma_\varepsilon}\right)\cdot\nabla\varepsilon\right) + P_\varepsilon - \mathrm{D}_\varepsilon \qquad (8)$$

$$P_k = \nabla\tilde{U} : \left(\mu_T\cdot\left(\left(\nabla\tilde{U}\right) + \left(\nabla\tilde{U}\right)^T - \frac{2}{3}\cdot\left(\nabla\cdot\tilde{U} - \bar{\rho}\cdot k\right)\cdot\boldsymbol{I}\right)\right) \qquad (10)$$

$$\mathrm{D}_k = \bar{\rho}\cdot\varepsilon \qquad (11)$$

$$P_\varepsilon = C_{e1}\cdot\left(\frac{\varepsilon}{k}\right)\cdot P_k \qquad (12) \qquad \mathrm{D}_\varepsilon = C_{e2}\cdot\bar{\rho}\cdot\left(\frac{\varepsilon^2}{k}\right) \qquad (13)$$

Temperature equation:

$$\bar{\rho}\cdot C_p\left(\frac{\partial \tilde{T}}{\partial t} + \left(\tilde{U}\cdot\nabla\right)\tilde{T}\right) = \nabla\cdot\left(\left(\lambda+\lambda_T\right)\cdot\nabla\tilde{T}\right) + \frac{\tilde{T}}{\bar{\rho}}\cdot\left(\frac{\partial\bar{\rho}}{\partial\tilde{T}}\right)_p\left(\frac{\partial\bar{p}}{\partial t} + \left(\tilde{U}\cdot\nabla\right)\bar{p}\right) + \left[\nabla\tilde{U} : \left(\left(\mu+\mu_T\right)\cdot\left(\left(\nabla\tilde{U}\right) + \left(\nabla\tilde{U}\right)^T - \frac{2}{3}\cdot\nabla\cdot\tilde{U}\cdot\boldsymbol{I}\right)\right)\right] \qquad (14)$$

Eddy viscosity:

$$\mu_T = \bar{\rho}\cdot C_\mu\cdot\left(\frac{k^2}{\varepsilon}\right) \qquad (15)$$

Dynamic viscosity (Sutherland's law):

$$\mu = \mu_{ref}\left(\frac{\tilde{T}}{T_{ref}}\right)^{\frac{3}{2}}\cdot\frac{\left(T_{ref}+S_\mu\right)}{\left(\tilde{T}+S_\mu\right)} \qquad (16)$$

Where μ_{ref} =1.448x10^{-5} and T_{ref} =221.65K pertaining to an altitude of 25km. The turbulent Prandtl number (Pr_T) for the high speed flow is chosen to be a constant value of 0.89 [4]. The thermal conductivity λ is obtained directly from material library and turbulent thermal conductivity is given by $\lambda_T = \frac{\mu_T}{Pr_T}$. The turbulent flow k-ε model constants are given in the **Table 3**.

C_μ	$C_{\varepsilon1}$	$C_{\varepsilon2}$	σ_k	σ_ε
0.09	1.44	1.92	1	1.3

Table 3: High Reynolds number k-ε model constants

4. Boundary and initial Conditions: The boundary conditions are chosen such that they mimic the atmospheric conditions that pertain to 25km [7]. While the model domain is initialised with free stream conditions which ensure a pulse start to avoid any event of unstart [3]. As k-ε model cannot capture viscous sub-layer, the numerical tool assumes an analytical solution for the same with appropriate wall distance δ_w^+ [13]. The boundary with normal vector **n** is subjected to conditions that are described in the equation (17-23):

i. Scramjet Wall: Wall function

$$\tau_w = -\bar{\rho} \cdot \frac{u_\tau \cdot \tilde{U}_{tang}}{\delta_w^+} \quad (17) \qquad \text{Where } \tilde{U}_{tang} = \tilde{U} - (\tilde{U} \cdot \boldsymbol{n})\boldsymbol{n}$$

$$k = \frac{u_\tau}{\sqrt{C_\mu}} \quad (18) \qquad \varepsilon = -\rho \cdot C_\mu \cdot \left(\frac{k^2}{0.41 \cdot \delta_w^+ \cdot \mu} \right) \quad (19) \qquad \tilde{U} \cdot \boldsymbol{n} = 0 \quad (20)$$

ii. Inlet: Characteristic based inlet conditions involving M_∞, P_∞, and T_∞ are prescribed on the inlet. The supersonic inlet as selected in Comsol Multiphysics ensures all these characteristics are pointing inward into the domain. The details of inlet conditions are specified in **Table 4**, refer [8]:

Free stream conditions	
Mach numbers (M_∞)	[4, 5]
Temperature (T_∞)	221.65K
Pressure (P_∞)	2511.023 Pa
Turbulence intensity ($T_{i\infty}$)	0.01
Viscosity ratio ($\frac{\mu_{T\infty}}{\mu_\infty}$)	10

Table 4: Inlet boundary conditions

iii. Outlet: The supersonic outlet as selected in Comsol Multiphysics ensures all the characteristic variables are pointing outward out of the domain. Also, gradients of turbulence parameters and temperature are nullified on the boundary which is described below mathematically:

a) $\nabla k \cdot \boldsymbol{n} = 0$ (21)

b) $\nabla \varepsilon \cdot \boldsymbol{n} = 0$ (22)

c) $\nabla T \cdot \boldsymbol{n} = 0$ (23)

5. Grid Generation and Solver: "Comsol Multi-physics" provides a wide variety of meshing and solver options. As the flow is characterised by shock waves, consequently high gradients of primary variables exist, to capture this, a two level adaptive meshing feature using L2 norm method for error estimation. The mesh elements used for numerical simulation are unstructured triangular mesh as shown in **Figure 4**. The boundary layer effect is captured by using 4 rectangular cell grids on boundaries with wall functions prescribed as explained in section **4**. The boundary layer mesh thickness and growth rate are varied accordingly for each case for desired result. The type of mesh interpolation or element order is selected in Comsol Multi-physics to be "P1+P1" which indicates first order element type to compute primary variables which is used for FEM computation.

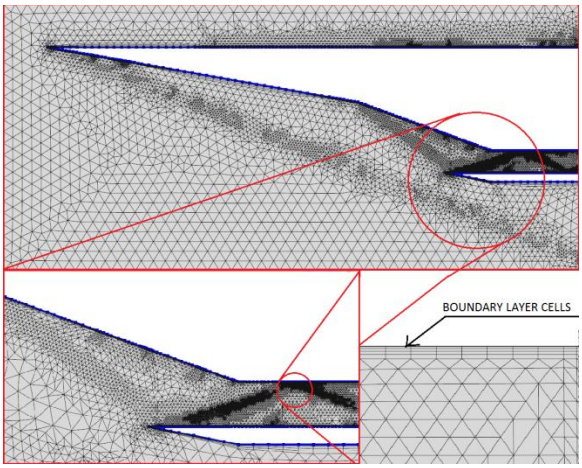

Figure 4: Adaptive mesh with boundary layer cells for Double ramp inlet (DR) having δ=0 with free stream Mach number M_∞=4.

Each case of turbulent solution is initialised with the prior solution obtained from Euler equations. All the primary variables while solving are fully coupled using pseudo time stepping with stationary solver. The stationary solver uses PARDISO (Parallel Sparse Direct Linear Solver) along with nested dissection multithreaded pre-ordering algorithm. The convergence the criteria was determined by setting the relative tolerance to 0.01 for all the cases.

6. Result and analysis: The performance parameters which are defined in section **1.1** are evaluated and tabulated to draw inference. Altogether for eight cases the numerical simulations were performed having four different geometries subjected to two free stream Mach numbers (4&5). Along with the analysis of performance parameters few other observations from the computational result are also discussed. To study the variation of the performance parameters with respect to change in three salient variables namely; inlet ramp contour, cowl angle and Mach number it is desired to evaluate the standard deviation of performance parameters with respect to each of these variables. The procedure that is implemented for a computing the standard deviation

for a performance parameter, say 'X' with respect to cowl angel (δ), is described by first calculating the global mean of X for all the eight cases.

$$\bar{X} = \frac{\left(\sum_{i=1}^{8} X\right)}{8} \quad (25)$$

Having calculated the global mean for all the eight cases, the local mean for each case of the variable δ [0^0, 10^0] is calculated.

$$\bar{X}_{\delta 0} = \frac{\sum_{i=1}^{4} X \Big|_{\delta = 0}}{4} \quad (26) \qquad \bar{X}_{\delta 10} = \frac{\sum_{i=5}^{8} X \Big|_{\delta = 10}}{4} \quad (27)$$

Now with $\bar{X}_{\delta 0}$, $\bar{X}_{\delta 10}$ and global mean as $\bar{X}$ the standard deviation X_D can be obtained from equation (28).

$$X_D = \sqrt{\frac{\left(\left(\bar{X}_{\delta 0} - \bar{X}\right)^2 + \left(\bar{X}_{\delta 10} - \bar{X}\right)^2\right)}{2}} \quad (28)$$

Similarly, evaluation of X_D with respect to Mach number and ramp contour is carried out.

6.1 Mass capture: The mass capture signifies the efficacy of the inlet in captivating the volume of air from the head stream which is then fuelled for combustion. The air capture ratio described in equation (1) as a performance parameter which quantifies the mass capture is tabulated in **Table 5**.

$X=m_c$	DR δ=0	DR δ=10	ICR δ=0	ICR δ=10
M_∞=4	0.7886	0.7193	0.7996	0.6793
M_∞=5	0.9433	0.8562	0.9964	0.8815

Table 5: Air capture ratio

It is evident from **Table 5** that numerical simulation predicts that the inlet designed with isentropic compression ramp with cowl completely open captivates maximum volume of air than compared to other cases at a given Mach number, while increasing the Mach number itself causes increase in air capture ratio. This can be reasoned out by referring to the surface plot of Mach number from which we notice that the "shock on lip" condition is almost sufficed for the designed inlet **Figure 3** with free stream Mach number 5 and δ=0 as observed in **Figure 11**. Albeit the bending of the cowl reduces the efficiency of mass capture which is substantiated by the decrease in A_C, it possesses its own advantage in performance **[12]**. To summarize the impact of the variables on air-capture ratio the X_D is tabulated in **Table 6**.

$X=m_c$	M_∞	Inlet Ramp	δ
X_D	0.08632	0.006175	0.04895

Table 6: Standard deviation for air capture ratio

Clearly from **Table 6**, the impact of Mach number jump from 4 to 5 on m_c is the highest but in reference to the geometrical impact, the cowl angle effectively hampers the air capture ratio with 10^0 turn as compared to the ameliorative action of isentropic compression ramp. It is to be noted that subtracting '1' from each values in **Table 5** will provide an insight in to spillage.

6.2 Total pressure efficiency: The total pressure efficiency signifies the irreversible losses that occur across the shock waves which are not favourable for combustion although it is inevitable in a hypersonic flight. Despite the present study is on low hypersonic limits, it is desired to mention that at higher limits the scramjet is designed to have very high contraction ratios in which the boundary layer thickens along the flow inside the isolator **[1]**, **[10]** creating subsonic regions through which the back pressure from combustion compounds the same thickening in turn causing an event of unstart **[3]** which engenders the augment of spillage. Therefore if the total pressure losses are kept minimum, the event of unstart can be avoided due to boundary layer thickness growth. The total pressure efficiency as described in equation (2) is tabulated in **Table 7**.

$X=\eta_P$	DR δ=0	DR δ=10	ICR δ=0	ICR δ=10
M_∞=4	0.8581	0.8537	0.8745	0.8584
M_∞=5	0.8753	0.8636	0.8918	0.8929

Table 7: Total pressure efficiency

From the **Table 7** it can be inferred that the numerical simulation predicts that the inlet designed with isentropic compression ramp suffer lesser total pressure losses as compared to double wedge ramp. This inference supports the fundamental shock-expansion theory **[6]** interpretation of total pressure loss across the shock. However the increase in free stream Mach number increases the free stream total pressure which has direct consequence on total pressure efficiency by augmenting it, whereas the effect of bending the cowl cannot be generalised as many other aspects are involved in it. To comprehend the effect of cowl angle on total pressure efficiency at the throat it may be delusive to base the reasoning only on shock-expansion (SE) theory. The SE theory only interprets the effect of two weaker shocks, in case of δ=10, to be more pressure efficient than one strong shock in δ=0 case, but many other complex interaction between shock, expansion fan and boundary layer that prevail at the throat are not substantiated by the same theory. Therefore from the observation of **Table 8** it can be concluded that a generalised trend cannot be drawn in regard to

change in cowl angle, but these observations from the same table may not hold good downstream inside the isolator [12]. To summarize the impact of the variables on total pressure efficiency the standard deviation is tabulated in **Table 8**.

$X=\eta_P$	M_∞	Inlet Ramp	δ
X_D	0.009862	0.008362	0.003887

Table 8: Standard deviation for air capture ratio

From **Table 8** the impact of Mach number jump from 4 to 5 on η_P is the highest but in the reference to the geometrical impact by changing the inlet ramp contour from DR to ICR has a greater effect than turning the cowl lip by 10^0.

6.3 Kinetic energy efficiency: The term η_{KE} is defined in the section **1.1** which quantifies the loss of kinetic energy by evaluating total (h_0), sensible (h) and isentropic (h^*) enthalpy at throat and free stream. These losses occur due to flow across shock and boundary layer. The total kinetic energy efficiency described in the in equation (3) as a performance parameter is tabulated in the **Table 9**.

$X=\eta_{KE}$	DR δ=0	DR δ=10	ICR δ=0	ICR δ=10
M_∞=4	0.8505	0.8421	0.8545	0.8425
M_∞=5	0.8443	0.8616	0.8753	0.8728

Table 9: Kinetic energy efficiency.

The review of the above table suggests that there are no drastic variations in the value of η_{KE} with respect any variable, also, no general trend of variation in η_{KE} with either δ or M_∞ is observed, but the variation of η_{KE} with inlet ramp contour reveals that ICR suffers lesser losses when compared to DR. To summarize the impact of the variables on total pressure efficiency X_D is tabulated in **Table 10**.

$X=\eta_{KE}$	M_∞	Inlet Ramp	δ
X_D	0.00805	0.00582	0.0007

Table 10: Standard deviation for kinetic energy efficiency.

In reference to **Table 10** it can be inferred that the impact of all the three variables are almost same while the nature of the impact are different. A complete interpretation in regard to energy can be drawn by inspecting the total heat loss at the throat which is defined as $\Delta Q_{loss} = h_{0\infty} - h_{0T}$ which is tabulated in **Table 11.** Therefore in reference to **Table 11** it can be concluded that that ICR suffers less energy losses as compared to DR.

ΔQ_{loss} J/kg	DR δ=0	DR δ=10	ICR δ=0	ICR δ=10
M_∞=4	44326	4632	39169	44607
M_∞=5	86974	91120	78030	75850

Table 11: Total heat loss ΔQ_{loss}(J/kg).

6.4 Aerodynamic drag: The standard representation of inlet drag is represented in its coefficient form as defined in equation (4). The values of C_D are tabulated in **Table 12**.

$X=C_D$	DR δ=0	DR δ=10	ICR δ=0	ICR δ=10
M_∞=4	0.4181	0.4879	0.4487	0.5346
M_∞=5	0.5630	0.6848	0.5523	0.6852

Table 12: Coefficient of drag for scramjet inlet.

It is lucid from **Table 12** that increase in Mach number augments the drag coefficient which can be substantiated by the shock-expansion theory interpretation, while the effect of turning cowl lip by 10^0 increases C_D. The cowl lip was designed to reduce the drag by designing its lower surface to be inclined **Figure 1** such that its more aligned with the incoming flow of 20^0 turn causing weak shock to occur below the cowl lip **Figure 5-12** which is expected to abate the drag [6] at the lip. This design of low drag cowl becomes redundant if the fore shock moves beyond the lip into the aft inlet. The observations based on inlet ramp contour indicate that ICR suffers slightly more drag than DR in most of the cases. To summarize the impact of the variables on coefficient the standard deviation is tabulated in **Table 13**.

$X=C_D$	M_∞	Inlet Ramp	δ
X_D	0.074500	0.008375	0.051300

Table 13: Standard deviation of Coefficient of drag.

It can be inferred from **Table 13** that Mach number jump from 4 to 5 impacts drag coefficient the most, but in reference to geometry, the change in cowl angle by 10^0 has more impact on C_D as compared to the effect of changing the inlet contour on the same. The effect of free stream turbulence [8] is prominently reflected in the boundary layer stresses which are best represented by skin friction coefficient defined as $C_f = \frac{\tau_w}{\frac{1}{2}\rho V_\infty^2}$ where τ_w is wall stress. The line- averaged $\bar{C}_f$ along the boundary of scramjet inlet wall are tabulated in **Table 14**, in reference to this table the increase in Mach number as expected augments the skin friction.

$X=\bar{C}_f$	DR δ=0	DR δ=10	ICR δ=0	ICR δ=10
M_∞=4	0.00238	0.00282	0.00234	0.00235
M_∞=5	0.00438	0.00431	0.00516	0.00526

Table 14: Averaged skin friction coefficient $\bar{C}_f$

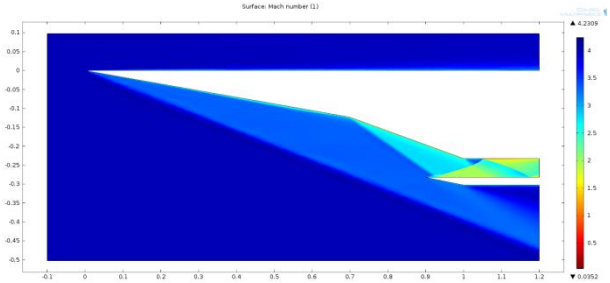

Figure 5 : Surface plot of M for Double Ramp inlet with cowl angle $\delta=0^0$ with free stream Mach number 4.

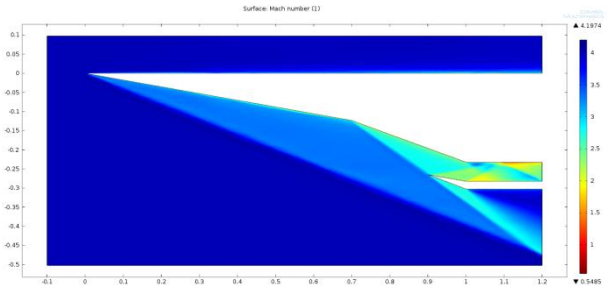

Figure 6: Surface plot of M for Double Ramp inlet with cowl angle $\delta=10^0$ with free stream Mach number 4.

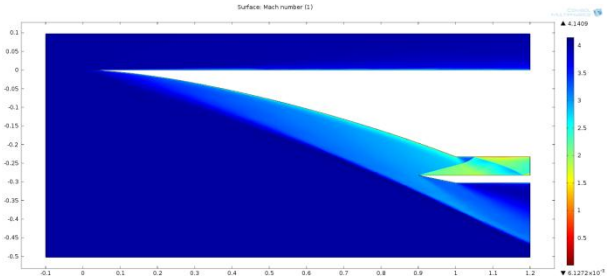

Figure 7: Surface plot of M for Smooth second degree curve Ramp inlet with cowl angle $\delta=0^0$ with free stream Mach number 4.

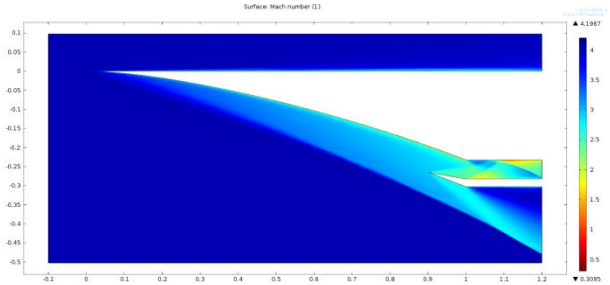

Figure 8: Surface plot of M for Smooth second degree curve Ramp inlet with cowl angle $\delta=10^0$ with free stream Mach number 4.

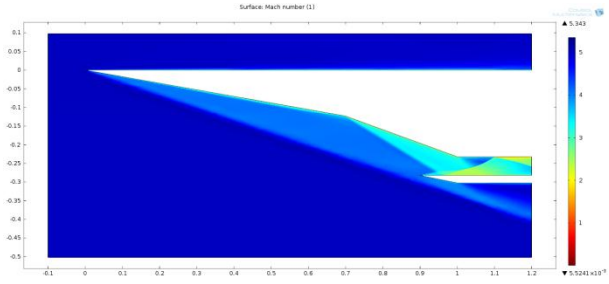

Figure 9: Surface plot of M for Double Ramp inlet with cowl angle $\delta=0^0$ with free stream Mach number 5.

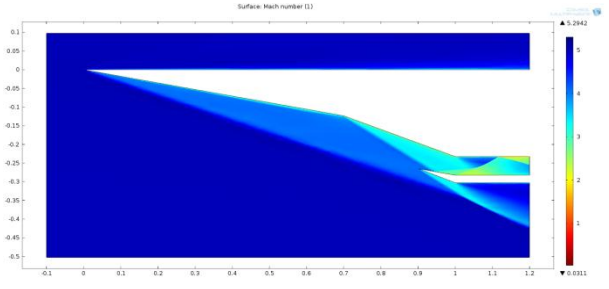

Figure 10: Surface plot of M for Double Ramp inlet with cowl angle $\delta=10^0$ with free stream Mach number 5.

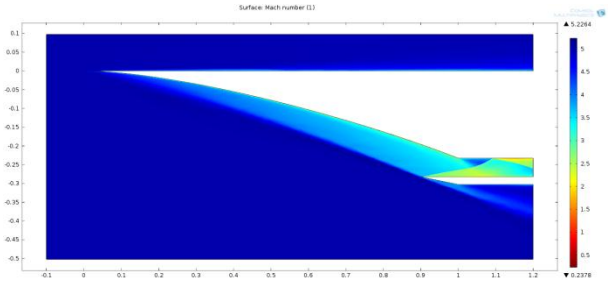

Figure 11: Surface plot of M for Smooth second degree curve Ramp inlet with cowl angle $\delta=0^0$ with free stream Mach number 5.

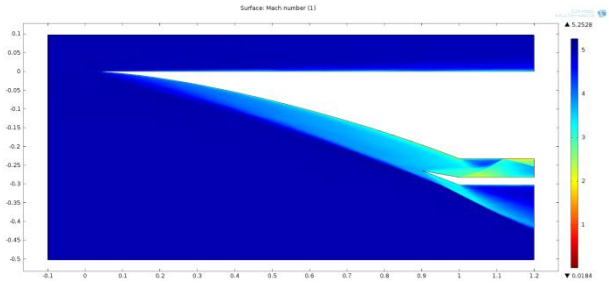

Figure 12: Surface plot of M for Smooth second degree curve Ramp inlet with cowl angle $\delta=10^0$ with free stream Mach number 5.

6.5 Additional Observations: The numerical simulation performed has captured important phenomenon that occur in inlet flow field such as shock boundary layer reflection accompanied with separation bubble which is plotted in **Figure 13**.

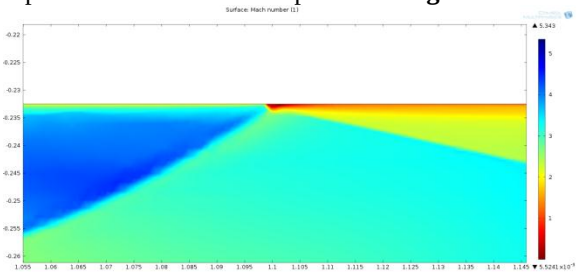

Figure 13: Surface plot for M which visualises Shock boundary layer reflection in which the deep red region of very low Mach number indicates separation bubble formation.

Also flow reversal and circulations were observed near shock boundary layer reflection reconfirming the presence of separation bubble. Although no occurrence of separation bubble at throat was observed, its presence at throat may abate the mass capture which is not desired **[5]**. Apart from the above observations the maximum wall temperatures (T_{MAX}) were recorded for each case which is tabulated in the table below

T_{MAX} K	DR δ=0	DRδ=10	ICR δ=0	ICR δ=10
M_∞=4	526.75	517.23	523.65	526.63
M_∞=5	615.52	609.23	613.65	607.38

Table 15: Maximum wall temperature T_{MAX} (K).

7. Conclusion: The evaluation of performance parameters from the numerical simulation predicts that inlet geometry designed with isentropic compression ramp **Figure 2** performs better than double ramp inlet **Figure 3** in lower hypersonic limits by providing favourable conditions for combustion as indicated by standard performance parameters. Although no definite conclusion can be drawn with regard to cowl angle, it can be said that the cowl lip rotation is essential for the inlet to adapt to various regimes of the hypersonic flight **[3]**, **[12]**. The result obtained in the present study and its analysis is applicable only to a similar or a congruent geometry to the geometry that has been proposed in this work. Thus the vital performance parameters obtained from the FEM numerical simulation are compared and analysed by parameterizing inlet ramp contour, Mach number and cowl angle at low hypersonic limits.

8. References:

[1]E.T. Curran, S.N.B Murthy, "Scramjet Propulsion", Progress in Astronautics and Aeronautics", AIAA Volume 189.

[2]Christopher J Roy and Frederick G Blottner, "Assessment of One- and Two-Equation Turbulence Models For Hypersonic Transitional Flows", Sandia National Laboratories, Albuquerque, New Mexico 87185,Journal of spacecraft and rockets, Vol.38,No.5,September October 2011.

[3] Donde P., Marathe A. G., Sudhakar K., "Starting in hypersonic intakes", 42nd AIAA/ASME/SAE/ASEE Joint Propulsion Conference, AIAA 2006-4510, 2006

[4]X.Xiao1, J.R. Edwards1, H. A. Hassan1, and R.L. Gaffeny,Jr2 "Role of Turbulent Prandtl Number on Heat Flux at Hypersonic Mach numbers", 1North Carolina state university Raleigh, 2NASA Langley Research Center Hampton, 43rd AIAA aerospace science meeting and exhibit, 10-13 Jan 2005, Nevada

[5]M. Krause, B.Reinartz, J.Ballmann, "NUMERICAL COMPUTATIONS FOR DESIGNING A SCRAMJET INTAKE", Department of mechanics, RWTH Aachen University. 25th International congress of aeronautical sciences, 2006.

[6]John D Anderson, Modern compressible flow, third edition, Mc Graw hill.

[7]US Standard atmosphere 1976, NOAA, NASA and USAF

[8]Christopher J. Roy, Frederick G. Blottner, "Methodology for Turbulence Model Validation: Application to hypersonic flow", Sandia National Laboratories, Albuquerque, New Mexico. Journals of spacecraft and rockets Vol.40, No. 3, May-June 2003.

[9] J.P. Drummond, G.S. Diskin, A.D. Cutler, Fuel–Air Mixing and Combustion in Scramjets, Technologies For Propelled Hypersonic Flight, Working Group AVT 10, Final Report, NATO Research and Technology Organization, 2001

[10][1]Heeseok Koo, [1]Ventkatramanan Raman, "DETAILED NUMERICAL SIMULATIONS OF A SUPERSONIC INLET-ISOLATOR" , [1]The University of Texas at Austin, Sixth International Symposium on Turbulence and Shear Flow Phenomena, Seoul, Korea, 2009.

[11]Derek J.Dalle, Sean M. Torrez, and James F. Driscoll, "Performance Analysis of Variable-Geometry Scramjet Inlets Using a Low-Order Model", University of Michigan, Ann Arbor, 47th AIAA/ASME/SAE/ASEE Joint propulsion Conference & Exhibit 31 July-03 August 2011, San Diego, California.

[12]Derek J. Dalle, Matt L. Fotia, and James F. Driscoll, "Reduced-Order Modeling of Two-Dimensional Supersonic Flow with Applications to Scramjet Inlets", University of Michigan, Ann Arbor, Michigan, Journal of propulsion and powe, Vol.26 No.3, May-June 2010.

[13]D.Kuzmin, O. Mierka, S. Turek, " On the implementation of the k-ε turbulence model in incompressible flow solvers based on finite element discretization", University of Dortmund, International Journal of Computing Science and Mathematics, Vol.1 Issue 2-4, Jan 2007, Pages 193-206.